

6-28-2018

Topological Nodal Line Semimetal in an Orthorhombic Graphene Network Structure

Jian-Tao Wang

Chinese Academy of Sciences; University of Chinese Academy of Sciences, wjt@aphy.iphy.ac.cn

Changfeng Chen

University of Nevada, Las Vegas, changfeng.chen@unlv.edu

Yoshiyuki Kawazoe

Tohoku University; SRM Institute of Science and Technology

Follow this and additional works at: https://digitalscholarship.unlv.edu/physastr_fac_articles



Part of the [Physics Commons](#)

Repository Citation

Wang, J., Chen, C., Kawazoe, Y. (2018). Topological Nodal Line Semimetal in an Orthorhombic Graphene Network Structure. *Physical Review B*, 97(24), 1-7.

<http://dx.doi.org/10.1103/PhysRevB.97.245147>

This Article is protected by copyright and/or related rights. It has been brought to you by Digital Scholarship@UNLV with permission from the rights-holder(s). You are free to use this Article in any way that is permitted by the copyright and related rights legislation that applies to your use. For other uses you need to obtain permission from the rights-holder(s) directly, unless additional rights are indicated by a Creative Commons license in the record and/or on the work itself.

This Article has been accepted for inclusion in Physics & Astronomy Faculty Publications by an authorized administrator of Digital Scholarship@UNLV. For more information, please contact digitalscholarship@unlv.edu.

Topological nodal line semimetal in an orthorhombic graphene network structure

Jian-Tao Wang,^{1,2,*} Changfeng Chen,³ and Yoshiyuki Kawazoe^{4,5}

¹Beijing National Laboratory for Condensed Matter Physics, Institute of Physics, Chinese Academy of Sciences, Beijing 100190, China

²School of Physics, University of Chinese Academy of Sciences, Beijing 100049, China

³Department of Physics and High Pressure Science and Engineering Center, University of Nevada, Las Vegas, Nevada 89154, USA

⁴New Industry Creation Hatchery Center, Tohoku University, Sendai 980-8579, Japan

⁵Department of Physics and Nanotechnology, SRM Institute of Science and Technology, Kattankulathur 603203, Tamil Nadu, India



(Received 9 February 2018; revised manuscript received 21 May 2018; published 28 June 2018)

Topological semimetals are a fascinating class of quantum materials that possess extraordinary electronic and transport properties. These materials have attracted great interest in recent years for their fundamental significance and potential device applications. Currently a major focus in this research field is to theoretically explore and predict and experimentally verify and realize material systems that exhibit a rich variety of topological semimetallic behavior, which would allow a comprehensive characterization of the intriguing properties and a full understanding of the underlying mechanisms. In this paper, we report on *ab initio* calculations that identify a carbon allotrope with simple orthorhombic crystal structure in $Pbcm$ (D_{2h}^{11}) symmetry. This carbon allotrope can be constructed by inserting zigzag carbon chains between the graphene layers in graphite or by a crystalline modification of a (3,3) carbon nanotube with a double cell reconstruction mechanism. Its dynamical stability has been confirmed by phonon and molecular dynamics simulations. Electronic band calculations indicate that it is a nodal-line semimetal comprising two nodal lines that go through the whole Brillouin zone in bulk and a projected surface flat band around the Fermi level. The present findings establish an additional topological semimetal system in the nanostructured carbon allotropes family and offer insights into its outstanding structural and electronic properties.

DOI: [10.1103/PhysRevB.97.245147](https://doi.org/10.1103/PhysRevB.97.245147)

I. INTRODUCTION

Carbon is capable of forming an extremely rich variety of structural allotropes due to the versatile hybridized bonding states of its $2s^2 2p^2$ valence electrons [1–5]. At ambient conditions, graphite is the most stable carbon phase; its honeycomb lattice can be viewed as a planar molecule comprising benzene rings in an all- sp^2 bonding state, which hosts a semimetallic electronic structure [6]. At high pressures, graphite can be converted into insulating cubic or hexagonal diamond at high temperatures [7–11] or diamondlike cold-compressed graphite phases at room temperature [12–19], such as *M*-carbon [14], bct- C_4 [15], and *W*-carbon [16] in all- sp^3 bonding. Modern advances in synthesis techniques have made it possible to convert graphitic carbon sheets into new structural forms, such as zero-dimensional fullerenes [20], one-dimensional nanotubes [21], two-dimensional (2D) graphene [22], and three-dimensional (3D) polybenzene [23,24] in all- sp^2 bonding. The well-known monolayer 2D graphene has a Dirac point in its 2D Brillouin zone (BZ), characterized as a nodal-point semimetal [25]. Recent theoretical studies suggested that 3D graphene networks support topological semimetals harboring continuous nodal lines that go through the whole BZ or nodal rings that reside inside a mirror plane of the BZ [26–36]. Topological semimetals with node rings have been found in all- sp^2 carbon network structures such as Mackay-Terrones

carbon crystal [26], body-centered orthorhombic C_{16} (bco- C_{16}) [29], and a body-centered tetragonal C_{16} (bct- C_{16}) [33]. Meanwhile topological semimetals with node lines have been found in sp^2 - sp^3 hybrid network structures such as interpenetrated graphene network C_6 (ign- C_6) [27], body-centered tetragonal C_{12} (bct- C_{12}) [28], and body-centered tetragonal C_{40} (bct- C_{40}) [34]. Moreover, 3D conductive interconnected graphene networks have been synthesized by chemical vapor deposition [37]. These advances open exciting avenues for constructing additional graphene framework structures.

In this paper, we report on a computational discovery of a carbon allotrope with simple orthorhombic crystal structure in $Pbcm$ (D_{2h}^{11}) symmetry, which can be constructed by inserting zigzag carbon chains between the graphene layers in graphite or by a crystalline modification of a (3,3) carbon nanotube (CNT) with a double cell reconstruction mechanism. The resulting interpenetrated graphene network structure contains 12 atoms in its unit cell, and is thus termed so- C_{12} . Total-energy calculations show that so- C_{12} is more stable than the polymeric (3,3) CNT and comparable to the recently reported ign- C_6 [27] and bct- C_{12} [28] network structures. Its dynamical stability has been verified by phonon mode analysis and molecular dynamics simulations. Electronic band-structure calculations show that so- C_{12} contains two mirror symmetric nodal lines in the bulk and one projected surface flat band around the Fermi level on its (010) surface. These findings place so- C_{12} as an additional member among topological node-line semimetals [38–52], and the results of the present paper are expected

*wjt@aphy.iphy.ac.cn

to help further understand and characterize these fascinating materials.

II. COMPUTATIONAL METHOD

Our calculations were carried out using the density functional theory as implemented in the Vienna *ab initio* simulation package [53]. The generalized gradient approximation (GGA) developed by Armiento-Mattsson (AM05) [54] was adopted for the exchange-correlation function for the structural relaxation. The all-electron projector augmented wave method [55] was adopted with $2s^22p^2$ treated as valence electrons. A plane-wave basis set with a large energy cutoff of 800 eV was used. Convergence criteria employed for both the electronic self-consistent relaxation and the ionic relaxation were set to 10^{-8} eV and 0.01 eV/Å for energy and force, respectively. The bulk and surface electronic band structures are calculated using the standard GGA-PBE method [56], while the band gaps are corrected using a hybrid density functional based on the Heyd-Scuseria-Ernzerhof scheme (HSE06) [57]. Phonon calculations were performed using the PHONOPY code [58]. The so-C₁₂ carbon structure is predicted in a double cell reconstruction pathway of (3,3) CNT based on a multistage phase transformation simulation method [59].

III. RESULTS AND DISCUSSION

We present in Fig. 1(a) the orthorhombic graphene network structure of so-C₁₂, which can be constructed by inserting zigzag carbon chains between the graphene layers in AA stacking along the *x* direction or AB stacking along the *y* direction. The calculated equilibrium lattice parameters are $a = 4.313$ Å, $b = 8.604$ Å, and $c = 2.461$ Å, occupying the $4d_1$ (0.0507, 0.2104, 0.25), $4d_2$ (0.0763, 0.0351, 0.25), and $4d_3$ (0.5783, 0.5052, 0.25) Wyckoff positions denoted by C₁, C₂, and C₃, respectively. The carbon atoms on the $4d_1$ and $4d_3$ sites form four zigzag carbon chains with aromatic sp^2 hybridization, while the carbon atoms on the $4d_2$ sites form two zigzag carbon chains with diamondlike sp^3 hybridization. Thus, there are three sets of distinct carbon-carbon bonds in this structure, namely, two sp^3 single longer bonds of 1.512 Å (C₂-C₃ and C₂-C₁) and 1.520 Å (C₂-C₂), and a shorter sp^2 aromatic bond of 1.406 Å (C₁-C₁ and C₃-C₃). There are also two sets of distinct bond angles—108.04° for $\angle C_2$ -C₂-C₂, 111.38° for $\angle C_2$ -C₂-C₁, and 111.04° for $\angle C_2$ -C₂-C₃, which are on average close to the 109.5° angle in diamond—and 118.95° for $\angle C_2$ -C₃-C₃, 118.90° for $\angle C_2$ -C₁-C₁, and 122.05° for $\angle C_3$ -C₃-C₃, which are on average close to the 120° angle in graphene.

It is noted that so-C₁₂ can be produced by a crystalline modification of (3,3) CNT. At the initial stage, the small (3,3) CNT can spontaneously turn into polymeric (3,3) CNT [60,61] under pressure (see Fig. S1 in Supplemental Material [62]). A double cell reconstruction pathway from polymeric (3,3) CNT toward so-C₁₂ is shown in Fig. 1(b) and the enthalpy versus pathway is plotted in Fig. 1(c) at 10 and 15 GPa. There are two sharp enthalpy peaks in Fig. 1(c). The first peak corresponds to the bond breaking between atoms 6-7 and 16-17 at step 9, followed by the enthalpy decrease with the rebonding

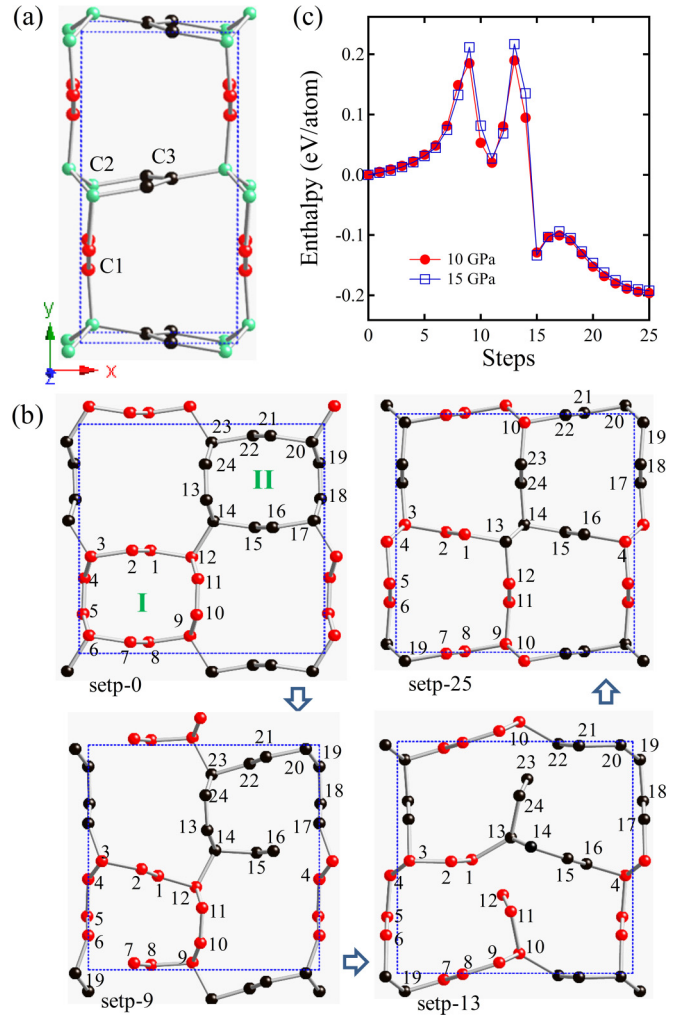


FIG. 1. The crystal structure of so-C₁₂ in $Pbcm$ (D_{2h}^{11}) symmetry. (a) The 12-atom unit cell of so-C₁₂ with lattice parameters $a = 4.313$ Å, $b = 8.604$ Å, and $c = 2.461$ Å, occupying the $4d_1$ (0.0507, 0.2104, 0.25), $4d_2$ (0.0763, 0.0351, 0.25), and $4d_3$ (0.5783, 0.5052, 0.25) Wyckoff positions denoted by C₁, C₂, and C₃, respectively. (b) A double cell reconstruction pathway from polymeric (3,3) CNT toward so-C₁₂ with bond breaking between atoms 6-7 and 16-17 at step 9 and between atoms 1-12 and 22-23 at step 13. The atoms are marked as red in tube I and black in tube II, respectively. The initial stage pathway from (3,3) CNT toward polymeric (3,3) CNT is shown in Fig. S1 in Supplemental Material [62]. (c) Enthalpy vs pathway from polymeric (3,3) CNT toward so-C₁₂ at 10 and 15 GPa.

between atoms 7-19 and 16-4 around step 11; the second peak corresponds to the bond breaking between atoms 1-12 and 22-23 at step 13, followed by the rebonding with atoms 13 and 10 with the bond rotation of atoms 13-14 and 9-10, respectively, to form the final so-C₁₂ structure. Throughout this *bond rotation assisted* two stage reconstruction pathway, the enthalpy barriers are estimated to be 0.19 – 0.22 eV [see Fig. 1(c)], which is similar to the findings in cold-compressed graphite phase transformations [16].

Figure 2 shows the total energy per atom as a function of volume for so-C₁₂ compared with the results for diamond, graphite, fcc-C₆₀ [63], ign-C₆ [27], bct-C₁₂ [28], bco-C₁₆ [29], bct-C₄ [15], *M*-carbon [14], and polymeric (3,3) CNT [61].

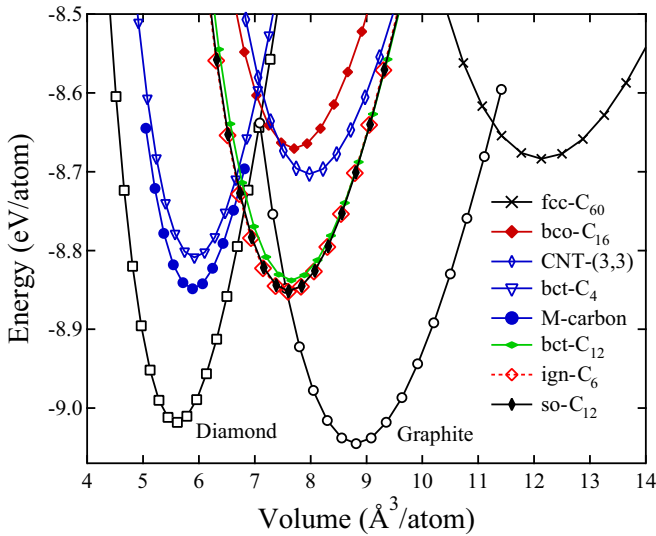


FIG. 2. Calculated energy vs volume per atom for so-C₁₂ compared to graphite, diamond, fcc-C₆₀ [63], bco-C₁₆ [29], bct-C₄ [15], M-carbon [14], bct-C₁₂ [28], ign-C₆ [27], and polymeric (3,3) CNT [61].

The results show that so-C₁₂ is slightly (0.16–0.19 eV per atom) higher in energy than diamond and graphite, while it is comparably stable as ign-C₆, bct-C₁₂, bct-C₄, and M-carbon, and more stable than bco-C₁₆, fcc-C₆₀, and polymeric (3,3) CNT. By fitting the calculated total energy as a function of volume to Murnaghan’s equation of state [64], we obtained the bulk modulus of 322 GPa for so-C₁₂, which is close to the results for bct-C₁₂ and ign-C₆ (see Table I) due to their similar atomic density and bonding nature.

For comparison, possible pathways from polymeric (3,3) CNT toward bct-C₁₂ and ign-C₆ are also simulated at 10 GPa (see Fig. S2 in Supplemental Material [62]). Along the pathway toward bct-C₁₂, there are four bond breakings between atoms 6–7, 1–12, 16–17, and 22–23 at step 11, resulting in an enthalpy barrier of 0.30 eV; meanwhile, along the pathway toward ign-C₆, the CNTs are squashed first with the tube rotation and then the squashed CNT-2 is inserted into CNT-1 at step 12, resulting in an enthalpy barrier of 0.34 eV. These enthalpy barriers are larger than the values of 0.19–0.22 eV for the pathway toward so-C₁₂. Thus so-C₁₂ is energetically more favorable compared to bct-C₁₂ and ign-C₆ in terms of the kinetics in the reconstruction pathway.

Since energetic calculations alone cannot establish the stability of a crystal structure, a thorough analysis of the dynamic and thermal stability is required. To assess the dynamical stability, we have calculated phonon dispersion and partial density of states (PDOS), and the obtained results are shown in Fig. 3. It is seen that there are two main peaks around 1443 and 1268 cm^{−1} in the PDOS. The peak around 1443 cm^{−1} is related to the C₁ and C₃ carbon atoms in *sp*² bonding similar to the finding in all-*sp*² bco-C₁₆ [29], while the peak around 1268 cm^{−1} is related to the C₂ carbon atoms in *sp*³ bonding similar to the finding in diamond [65]. There are also some peaks below 800 cm^{−1} related to the C₁, C₂, and C₃ carbon atoms in *sp*²-*sp*³ hybrid bonds. No imaginary frequency exists in the entire BZ and PDOS, confirming the dynamical stability

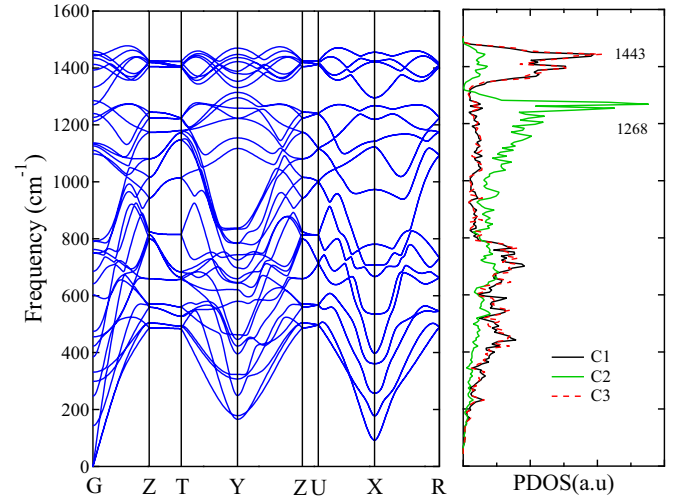


FIG. 3. Phonon band structures and partial density of states (PDOS) for so-C₁₂. The peaks around 1443 and 1268 cm^{−1} are related to *sp*² and *sp*³ bonding, respectively.

of so-C₁₂. To examine the thermal stability, we have performed *ab initio* molecular dynamics (AIMD) simulations with the canonical (*NVT*) ensemble by the Nosé thermostat [66] with a step of 1 fs. The systems are modeled by a 4 × 2 × 1 supercell. The energy fluctuations at 1200 and 1500 K are presented in Fig. 4. The structures around step 1000 and 4000 are given in the insets of Fig. 4. It is seen that after heating up to 1200 K for 4 ps no structural changes occur. With temperature increasing up to 1500 K, the structure becomes unstable with some bond breaking between the C₁-C₂ and C₂-C₃ bonds. These

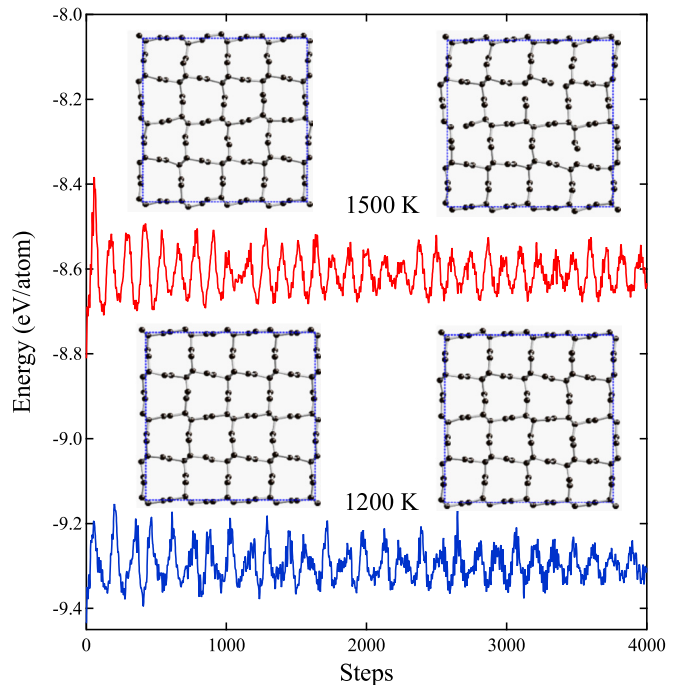


FIG. 4. Energy fluctuations of so-C₁₂ in AIMD simulations at 1200 and 1500 K. Insets depict the structural changes at step 1000 and 4000 during the simulations.

TABLE I. Calculated equilibrium structural parameters (space group; volume V_0 ; lattice parameters a , b , and c ; bond lengths d_{C-C}), total energy E_{tot} , bulk modulus B_0 , and electronic band gap E_g for diamond, polymeric CNT-(3,3), bco-C₁₆, bct-C₁₂, ign-C₆, so-C₁₂ and graphite, compared to available experimental data for diamond and graphite [7].

Structure	Method	V_0 (Å ³ /atom)	a (Å)	b (Å)	c (Å)	d_{C-C} (Å)	E_{tot} (eV)	B_0 (GPa)	E_g (eV)
Diamond ($Fd\bar{3}m$)	AM05	5.60	3.552			1.538	−9.018	451	5.36
	Exp. [7]	5.67	3.567			1.544		446	5.47
CNT-(3,3) ($Imma$)	AM05	7.98	8.536	2.485	9.025	1.338–1.566	−8.703	304	0.32
bco-C ₁₆ ($Imma$)	AM05	7.70	7.806	4.877	3.237	1.382–1.459	−8.671	315	Semimetal
bct-C ₁₂ ($I4/mcm$)	AM05	7.66	8.645	8.645	2.460	1.406–1.517	−8.838	320	Semimetal
ign-C ₆ ($Cmcm$)	AM05	7.60	5.899	6.281	2.459	1.406–1.522	−8.852	323	Semimetal
so-C ₁₂ ($Pbcm$)	AM05	7.61	4.313	8.604	2.461	1.406–1.520	−8.851	322	Semimetal
Graphite ($P6_3/mmc$)	AM05	8.81	2.462		6.710	1.422	−9.045	280	Semimetal
	Exp. [7]	8.78	2.460		6.704	1.420		286	

results indicate that so-C₁₂, once synthesized, can sustain high temperatures up to 1200 K.

Finally we discuss the electronic properties of so-C₁₂. Figure 5(a) shows the calculated bulk band structure at equilibrium lattice parameters. It is seen that the valence and conduction bands exhibit linear dispersion near the Fermi energy and cross at the Fermi level (E_F) to form several nodal points along the high-symmetric directions of G - Z , T - Y , and Y - Z in the bulk BZ. Further analysis of the band structure in the full BZ indicates that the band crossing points (or nodal points) of the valence and conduction bands in so-C₁₂ form two discrete *saddle* nodal lines inside a mirror plane G - Z - T - Y [see Fig. 5(b)] with an inversion symmetry about the center of G in the bulk BZ. The states near the crossing points around the nodal lines are formed by the inversion of the valence and conduction bands. To clarify this point, we have calculated the band decomposed charge density near the nodal point b on the high-symmetric direction T - Y in the BZ [see Fig. 5(c)]. One can see that the charges around the nodal points near the Fermi level are located on the C_1 and C_3 atoms and show the π -band character related to the p orbitals. The charge distributions for b_1 (and b_4) are 53.3% from C_1 - p_x and 45.1% from C_3 - p_y , while for b_2 (and b_3) the values are 49.3% from C_1 - p_x and 49.3% from C_3 - p_y orbitals. The obvious difference between the charge distributions of $b_1(b_4)$ and $b_2(b_3)$ reveals the inversion of the valence and conduction bands on both the left and right side of the nodal point. This band inversion can be described by two crossing π bands of G_1 and G_2 throughout the full BZ around the nodal lines. Furthermore, these node lines are protected by the coexistence of time-reversal (T) and spatial inversion (P) symmetry [26]. It is also noted that the spin-orbit coupling may open up a gap at the band crossing points, but the extremely weak (0.13–0.74 meV) coupling strength in carbon [26,29,30] is not expected to alter the semimetallic state at room temperature.

Figures 5(d) and 5(e) show the surface band structures calculated using a ten-layer-thick slab geometry along the [010] crystalline direction [see Fig. 5(f)]. The surface dangling bonds in Fig. 5(e) are saturated with hydrogen atoms. The projected surface BZ \bar{G} - \bar{Z} - \bar{T} - \bar{Y} is marked corresponding to G - Z - T - Y in bulk as shown in Fig. 5(b). It is seen that when the resulted nodal lines are projected onto the surface BZ they can

produce one topologically protected surface flat band around the Fermi level, either outside [the region containing the BZ boundaries in Fig. 4(e)] or inside [the region containing the \bar{G} point in Fig. 5(d)] of two symmetric (up and down) nodal lines, depending on the termination of the surface with or without saturation by hydrogen atoms. In Fig. 5(f) the partial charge density isosurfaces related to the energy bands around the Fermi level in Fig. 5(d) at the \bar{G} point are plotted. The electronic charges are located on the topmost surface carbon layers, confirming that the surface flat band is indeed deriving from the surface atoms. Beside the surface with the outermost atoms of C_2 and C_3 used in Figs. 5(d) and 5(e), there is another truncated surface with the outermost atoms of C_1 . The calculated surface band structures show similar surface states as plotted in Fig. S3 in Supplemental Material [62]. These surface states predicted for the nodal-line semimetals should be detectable by photoelectron spectroscopy and be compared to ARPES experimental data [50].

As a topological nodal-line semimetal, the nodal-line structure is usually protected by the topological invariant, i.e., the Berry phase (a \mathbb{Z}_2 -type invariant) along a closed path encircling the nodal line [67]. To clarify this point, we have calculated the Berry phase using the Wannier Tools package [68] based on a Wannier tight-binding model constructed by WANNIER90 [69]. The Berry phase with a closed loop surrounding the nodal lines (see Fig. S4(c) in Supplemental Material [62]) is calculated to be π . Further, the Berry phase along the line passing through the BZ parallel to the k_y axis is calculated. If the line is inside the area between two separated nodal lines (see Fig. S4(b) in Supplemental Material [62]), the result is either zero or π . The nonzero quantized Berry phase further confirms the nodal-line feature in so-C₁₂ carbon. The appearance of surface states at the surface of a nodal-line semimetal arises from a quantized Berry phase. Since the Berry phase is equal to π for any closed path that interlinks with the nodal line, the surface states should connect the a and b points on the projected nodal loop in the 2D momentum space in Figs. 5(d) and 5(e) since the surface states and the nodal line in bulk are at the same energy level.

According to the classification of topological nodal-line semimetals recently suggested by Hyart *et al.* [67], topological semimetals in 3D graphene networks can be divided into two types: type A has closed nodal rings that reside inside a mirror

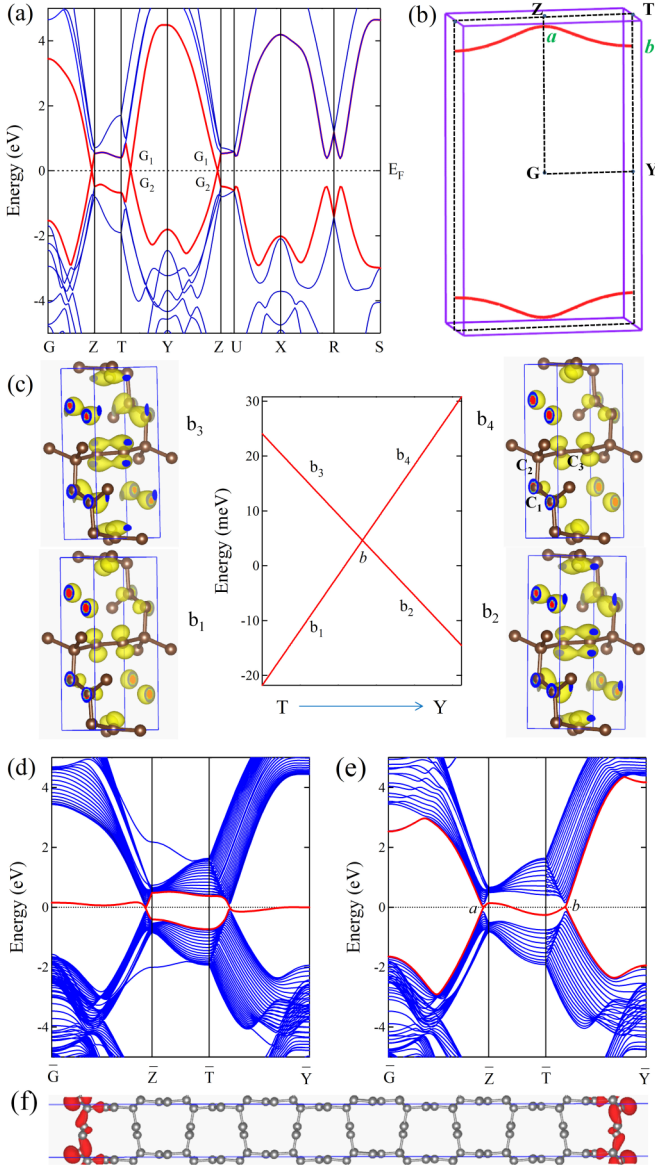


FIG. 5. Calculated bulk and surface band structures of so- C_{12} at equilibrium lattice parameters. (a) The bulk band structure along several high-symmetry directions. G_1 and G_2 indicate the irreducible representations of the two crossing bands, respectively. (b) The Brillouin zone (BZ) with several high-symmetry momenta indicated, and the nodal lines (red), formed by the band crossing points, in the G - Z - T - Y mirror plane. The a and b points represent the nodal point located along the G - Z and T - Y line, respectively. (c) The band-decomposed charge density isosurfaces ($0.07 e/\text{\AA}^3$) around the nodal point b along the T - Y direction in the BZ. (d,e) The (010) surface states obtained using a ten-layer-thick slab geometry along the $[010]$ direction. The surface flat band (red line) can be inside or outside the surface projected nodal lines, depending on the termination of the surface without (d) or with (e) saturation by hydrogen atoms. The projected surface BZ \bar{G} - \bar{Z} - \bar{T} - \bar{Y} is marked relative to G - Z - T - Y in bulk in (b). (f) Partial charge density isosurfaces ($0.05 e/\text{\AA}^3$) related to the (red) surface bands in (d) at the \bar{G} point. The outermost atoms are C_2 and C_3 with dangling bonds on C_2 sites.

plane of the BZ, while type B has continuous nodal lines that go through the whole BZ. The type-A nodal-line semimetals have been found in all- sp^2 carbon network structures such as bco- C_{16} [29] and bct- C_{16} [33]. The so- C_{12} reported in this paper has a type-B nodal line in the sp^2 - sp^3 hybrid network like that in ign- C_6 [27] and mC16 [36]. When the nodal line is projected onto certain surfaces, it produces a drumheadlike surface flat bands either inside or outside of the nodal lines [29]. Meanwhile, bct- C_{40} [34] is a nodal-net semimetal consisting of type-B nodal lines in the sp^2 - sp^3 hybrid network structure and has two coupled drumheadlike flat bands around the Fermi level on its surface. Beside these nodal-line or nodal-net semimetals, the 3D Weyl-surface semimetals are also reported in triangular graphene network TGN(2,2) [35], quadrilateral graphene network QGN(2,2) [35], and hexagonal graphene network HGN(2,2) [35]. It should be noted that such Weyl surfaces are closely related to an additional sublattice-symmetry operator in the tight-binding model [35], in contrast to the nodal nets reported in bct- C_{40} [34]. A similar Dirac surface was also reported in the higher-symmetry bct- C_{12} [28], but it should decay into type-B nodal lines in the lower-symmetry so- C_{12} phase reported here.

IV. CONCLUSION

In conclusion, we have identified by *ab initio* calculations a simple orthorhombic carbon allotrope in $Pbcm$ (D_{2h}^{11}) symmetry. This so- C_{12} carbon phase can be characterized as an interconnected graphene network structure containing 12 atoms in its unit cell and possibly synthesized by inserting zigzag carbon chains between the graphene layers in graphite or by a crystalline modification of the (3,3) carbon nanotube with a double cell reconstructing mechanism. Electronic band structure calculations reveal that so- C_{12} belongs to B-type topological nodal-line semimetals and possesses two periodically continuous lines in momentum space. Moreover, when the nodal lines in bulk are projected onto the surface BZ, they produce one topologically protected surface flat band around the Fermi level, either outside or inside of two symmetric nodal lines, depending on the termination of the surface with or without saturation by hydrogen atoms. The present results establish an additional nanostructured carbon phase that is expected to contribute to further characterization of structural and electronic properties and a full understanding of the underlying mechanisms in a large class of topological semimetals.

ACKNOWLEDGMENTS

The authors thank Dr. Hongming Weng for valuable discussions and help on the Berry phase calculation. This paper was supported by the National Natural Science Foundation of China (Grant No. 11674364) and the Strategic Priority Research Program of the Chinese Academy of Sciences (Grant No. XDB07000000). C.F.C. acknowledges support by the U.S. Department of Energy under Cooperative Agreement No. DE-NA0001982.

- [1] E. A. Belenkov and V. A. Greshnyakov, *Phys. Solid State* **55**, 1754 (2013).
- [2] R. H. Baughman, H. Eckhardt, and M. Kertesz, *J. Chem. Phys.* **87**, 6687 (1987).
- [3] J. T. Wang, C. F. Chen, H. D. Li, H. Mizuseki, and Y. Kawazoe, *Sci. Rep.* **6**, 24665 (2016).
- [4] A. San-Miguel and P. Toulemonde, *High Press. Res.* **25**, 159 (2005).
- [5] J. T. Wang, C. F. Chen, H. Mizuseki, and Y. Kawazoe, *Phys. Chem. Chem. Phys.* **20**, 7962 (2018).
- [6] G. P. Mikitik and Yu. V. Sharlai, *Phys. Rev. B* **73**, 235112 (2006).
- [7] F. Occelli, P. Loubeyre, and R. Letoullec, *Nat. Mater.* **2**, 151 (2003).
- [8] R. Clarke and C. Uher, *Adv. Phys.* **33**, 469 (1984).
- [9] I. Irifune, A. Kurio, S. Sakamoto, T. Inoue, and H. Sumiya, *Nature (London)* **421**, 599 (2003).
- [10] S. Scandolo, M. Bernasconi, G. L. Chiarotti, P. Focher, and E. Tosatti, *Phys. Rev. Lett.* **74**, 4015 (1995).
- [11] P. Németh, L. A. J. Garvie, T. Aoki, N. Dubrovinskaia, L. Dubrovinsky, and P. B. Buseck, *Nat. Commun.* **5**, 5447 (2014).
- [12] W. L. Mao, H. K. Mao, P. J. Eng, T. P. Trainor, M. Newville, C. C. Kao, D. L. Heinz, J. Shu, Y. Meng, and R. J. Hemley, *Science* **302**, 425 (2003).
- [13] H. Y. Niu, X. Q. Chen, S. B. Wang, D. Z. Li, W. L. Mao, and Y. Y. Li, *Phys. Rev. Lett.* **108**, 135501 (2012).
- [14] Q. Li, Y. M. Ma, A. R. Oganov, H. B. Wang, H. Wang, Y. Xu, T. Cui, H. K. Mao, and G. T. Zou, *Phys. Rev. Lett.* **102**, 175506 (2009).
- [15] K. Umemoto, R. M. Wentzcovitch, S. Saito, and T. Miyake, *Phys. Rev. Lett.* **104**, 125504 (2010).
- [16] J. T. Wang, C. F. Chen, and Y. Kawazoe, *Phys. Rev. Lett.* **106**, 075501 (2011).
- [17] J. T. Wang, C. F. Chen, and Y. Kawazoe, *J. Chem. Phys.* **137**, 024502 (2012).
- [18] M. Amsler, J. A. Flores-Livas, L. Lehtovaara, F. Balima, S. A. Ghasemi, D. Machon, S. Pailhes, A. Willand, D. Caliste, S. Botti, A. San Miguel, S. Goedecker, and M. A. L. Marques, *Phys. Rev. Lett.* **108**, 065501 (2012).
- [19] Z. S. Zhao, F. Tian, X. Dong, Q. Li, Q. Q. Wang, H. Wang, X. Zhong, B. Xu, D. L. Yu, J. L. He, H. T. Wang, Y. M. Ma, and Y. J. Tian, *J. Am. Chem. Soc.* **134**, 12362 (2012).
- [20] H. W. Kroto, J. R. Heath, S. C. O'Brien, R. F. Curl, and R. E. Smalley, *Nature (London)* **318**, 162 (1985).
- [21] S. Iijima, *Nature (London)* **354**, 56 (1991).
- [22] K. S. Novoselov, A. K. Geim, S. V. Morozov, D. Jiang, Y. Zhang, S. V. Dubonos, I. V. Grigorieva, and A. A. Firsov, *Science* **306**, 666 (2004).
- [23] J. T. Wang, C. F. Chen, E. G. Wang, and Y. Kawazoe, *Sci. Rep.* **4**, 4339 (2014).
- [24] H. A. Calderon, I. Estrada-Guel, F. Alvarez-Ramirez, V. G. Hadjiev, and F. C. Robles-Hernandez, *Carbon* **102**, 288 (2016).
- [25] M. Z. Hasan and C. L. Kane, *Rev. Mod. Phys.* **82**, 3045 (2010).
- [26] H. Weng, Y. Liang, Q. Xu, R. Yu, Z. Fang, X. Dai, and Y. Kawazoe, *Phys. Rev. B* **92**, 045108 (2015).
- [27] Y. P. Chen, Y. E. Xie, S. A. Yang, H. Pan, F. Zhang, M. L. Cohen, and S. B. Zhang, *Nano Lett.* **15**, 6974 (2015).
- [28] X. Dong, M. Hu, J. L. He, Y. J. Tian, and H. T. Wang, *Sci. Rep.* **5**, 10713 (2015).
- [29] J. T. Wang, H. Weng, S. Nie, Z. Fang, Y. Kawazoe, and C. F. Chen, *Phys. Rev. Lett.* **116**, 195501 (2016).
- [30] Y. Cheng, J. Du, R. Melnik, Y. Kawazoe, and B. Wen, *Carbon* **98**, 468 (2016).
- [31] B. Yang, H. C. Zhou, X. M. Zhang, X. B. Liu, and M. W. Zhao, *Carbon* **113**, 40 (2017).
- [32] C. Y. Zhong, Y. P. Chen, Z. M. Yu, Y. Xie, H. Wang, S. A. Yang, and S. B. Zhang, *Nat. Commun.* **8**, 15641 (2017).
- [33] Y. Cheng, X. Feng, X. T. Cao, B. Wen, Q. Wang, Y. Kawazoe, and P. Jena, *Small* **13**, 1602894 (2017).
- [34] J. T. Wang, S. M. Nie, H. Weng, Y. Kawazoe, and C. F. Chen, *Phys. Rev. Lett.* **120**, 026402 (2018).
- [35] C. Y. Zhong, Y. P. Chen, Y. Xie, S. A. Yang, Marvin L. Cohenc, and S. B. Zhang, *Nanoscale* **8**, 7232 (2016).
- [36] X. Feng, Q. S. Wu, Y. Cheng, B. Wen, Q. Wang, Y. Kawazoe, and P. Jena, *Carbon* **127**, 527 (2018).
- [37] Z. Chen, W. Ren, L. Gao, B. Liu, S. Pei, and H. Cheng, *Nat. Mater.* **10**, 424 (2011).
- [38] A. A. Burkov, M. D. Hook, and L. Balents, *Phys. Rev. B* **84**, 235126 (2011).
- [39] M. Phillips and V. Aji, *Phys. Rev. B* **90**, 115111 (2014).
- [40] C. Fang, Y. Chen, H. Y. Kee, and L. Fu, *Phys. Rev. B* **92**, 081201 (2015).
- [41] Y. Kim, B. J. Wieder, C. L. Kane, and A. M. Rappe, *Phys. Rev. Lett.* **115**, 036806 (2015).
- [42] R. Yu, H. Weng, Z. Fang, X. Dai, and X. Hu, *Phys. Rev. Lett.* **115**, 036807 (2015).
- [43] T. T. Heikkilä and G. E. Volovik, *New J. Phys.* **17**, 093019 (2015).
- [44] K. Mullen, B. Uchoa, and D. T. Glatzhofer, *Phys. Rev. Lett.* **115**, 026403 (2015).
- [45] L. S. Xie, L. M. Schoop, E. M. Seibel, Q. D. Gibson, W. Xie, and R. J. Cava, *APL Mater.* **3**, 083602 (2015).
- [46] Y.-H. Chan, C.-K. Chiu, M. Y. Chou, and A. P. Schnyder, *Phys. Rev. B* **93**, 205132 (2016).
- [47] T. Bzdušek, Q. Wu, A. Ruegg, M. Sigrist, and A. A. Soluyanov, *Nature (London)* **538**, 75 (2016).
- [48] Z. Yan and Z. Wang, *Phys. Rev. Lett.* **117**, 087402 (2016).
- [49] C.-K. Chan, Y.-T. Oh, J. H. Han, and P. A. Lee, *Phys. Rev. B* **94**, 121106 (2016).
- [50] G. Bian, T. R. Chang, R. Sankar, S.-Y. Xu, H. Zheng, T. Neupert, C.-K. Chiu, S.-M. Huang, G. Chang, I. Belopolski, D. S. Sanchez, M. Neupane, N. Alidoust, C. Liu, B. Wang, H.-T. Jeng, A. Bansil, F. Chou, H. Lin, and M. Z. Hasan, *Nat. Commun.* **7**, 10556 (2016).
- [51] C. L. Zhang, Z. J. Yuan, G. Bian, S. Y. Xu, X. Zhang, M. Z. Hasan, and S. Jia, *Phys. Rev. B* **93**, 054520 (2016).
- [52] M. Ezawa, *Phys. Rev. Lett.* **116**, 127202 (2016).
- [53] G. Kresse and J. Furthmüller, *Phys. Rev. B* **54**, 11169 (1996).
- [54] R. Armiento and A. E. Mattsson, *Phys. Rev. B* **72**, 085108 (2005).
- [55] P. E. Blöchl, *Phys. Rev. B* **50**, 17953 (1994).
- [56] J. P. Perdew, K. Burke, and M. Ernzerhof, *Phys. Rev. Lett.* **77**, 3865 (1996).
- [57] J. Heyd, G. E. Scuseria, and M. Ernzerhof, *J. Chem. Phys.* **124**, 219906 (2006).
- [58] A. Togo, F. Oba, and I. Tanaka, *Phys. Rev. B* **78**, 134106 (2008).
- [59] J. T. Wang, C. F. Chen, H. Mizuseki, and Y. Kawazoe, *Phys. Rev. Lett.* **110**, 165503 (2013).
- [60] C. S. Lian and J. T. Wang, *J. Chem. Phys.* **140**, 204709 (2014).
- [61] The polymeric (3, 3) CNT can be formed spontaneously from (3, 3) CNT based on an intertube sliding-assisted cross-linking mechanism under pressure [60]. The polymerization pathway is shown in Fig. S1 in Supplemental Material [62]. It contains two

- (3, 3) CNTs in $Imma$ (D_{2h}^{28}) symmetry [see Fig. 1(b)]. The lattice parameters are $a = 8.536$ Å, $b = 2.485$ Å, and $c = 9.025$ Å, occupying the $8i$ (0.4216, 0.25, 0.2341), $8i$ (0.1979, 0.25, 0.5374), and $8i$ (0.1711, 0.25, 0.7057) Wyckoff positions. It is a semiconductor with a direct band gap of 0.32 eV at the R point of the Brillouin zone.
- [62] See Supplemental Material at <http://link.aps.org/supplemental/10.1103/PhysRevB.97.245147> for the initial stage pathway from (3, 3) CNT toward polymeric (3, 3) CNT (Fig. S1); the enthalpy changes versus pathway from polymeric (3, 3) CNT toward bet- C_{12} and ign- C_6 at 10 GPa (Fig. S2); calculated surface band structures for the surface with the outermost atoms of C_1 (Fig. S3); and band structures and Berry phase result (Fig. S4) based on a tight-binding model.
- [63] W. I. F. David, R. M. Ibberson, J. C. Matthewman, K. Prassides, T. J. S. Dennis, J. P. Hare, H. W. Kroto, R. Taylor, and D. R. M. Walton, *Nature (London)* **353**, 147 (1991).
- [64] F. D. Murnaghan, *Proc. Natl. Acad. Sci. USA* **30**, 244 (1944).
- [65] J. T. Wang, C. F. Chen, D. S. Wang, H. Mizuseki, and Y. Kawazoe, *J. Appl. Phys.* **107**, 063507 (2010).
- [66] S. Nosé, *J. Chem. Phys.* **81**, 511 (1984).
- [67] T. Hyart, R. Ojajarvi, and T. T. Heikkila, *J. Low Temp. Phys.* **191**, 35 (2018).
- [68] Q. S. Wu, S. N. Zhang, H. F. Song, M. Troyer, and A. A. Soluyanov, *Comput. Phys. Commun.* **224**, 405 (2018).
- [69] A. A. Mostofi, J. R. Yates, Y.-S. Lee, I. Souza, D. Vanderbilt, and N. Marzari, *Comput. Phys. Commun.* **178**, 685 (2008).